

# Spatio-temporal spin transport from first principles

Mayada Fadel,<sup>1</sup> Joshua Quinton,<sup>2</sup> Mani Chandra,<sup>3</sup> Mayank Gupta,<sup>4</sup> Yuan Ping,<sup>4,\*</sup> and Ravishankar Sundararaman<sup>1,†</sup>

<sup>1</sup>*Department of Materials Science and Engineering,  
Rensselaer Polytechnic Institute, Troy, New York 12180, USA*

<sup>2</sup>*Department of Physics, Applied Physics, and Astronomy,  
Rensselaer Polytechnic Institute, Troy, New York 12180, USA*

<sup>3</sup>*nOhm Devices, Inc., Cambridge, MA 02138, USA*

<sup>4</sup>*Department of Materials Science and Engineering,  
University of Wisconsin–Madison, Madison, WI 53706, USA*

(Dated: May 13, 2025)

We introduce a computational framework for first-principles density matrix transport within the Wigner function formalism to predict transport of quantum-mechanical degrees of freedom such as spin over long time and length scales. This framework facilitates simulation of spin dynamics and transport from first principles, while accounting for electron-phonon scattering at device length scales. We demonstrate this framework to elucidate the impact of various spin-orbit field profiles, such as Rashba and persistent spin helix, on coherent spin transport in several materials. Using graphene under an electric field as an example to illustrate the impact of electron-phonon scattering on incoherent transport, we show how the transport changes with the strength of scattering. We identify three distinct regimes of incoherent spin transport corresponding to the free induction decay, Dyakonov-Perel and Elliott-Yafet regimes of spin relaxation. In particular, we show that the spin diffusion length is insensitive to the strength of scattering within the Dyakonov-Perel regime.

Accurate simulation of spin dynamics and transport is fundamental for understanding and controlling spintronic devices, which utilize the electron spins for information storage and processing [1]. By simulating spin transport, researchers can explore how spin information is carried and manipulated within materials, which is essential for designing more efficient and powerful spintronic devices. Desired materials used in spintronics need to have large spin relaxation times, spin diffusion lengths and spin Hall angles [2]. Accurate simulation techniques are needed to predict these quantities and understand the different relaxation mechanisms affecting them. They also need to account for phonons and electron-phonon interactions at device length scales in order to capture the effects of temperature.

Approaches to perform spin transport simulations range from non-equilibrium Green's functions methods suitable for first-principles transport on the molecular scale [3–5] to semi-empirical methods for longer length scales based on tight-binding models with scattering introduced by temperature-induced lattice and spin disorder [6, 7]. However, these approaches cannot yet explicitly account for phonons and electron-phonon coupling from first principles, while also targeting realistic length scales and geometries for spintronic devices, which is necessary for computational materials design.

In this Letter, we generalize first-principles density matrix dynamics simulations [8–11] to include spatial resolution within the Wigner function formalism. Using this framework, we can explicitly account for electron-phonon scattering at device length scales, can be generally applied to any material as it does not require the parameterization necessary for semi-empirical methods. We first show ballistic transport results for different materials

having various spin-orbit field profiles, where we observe dephasing due to transport in the absence of scattering, a distinctive feature of the spatially-resolved spin transport due to path-length differences between the electrons. We then take graphene with an applied electric fields as a prototypical example to investigate incoherent transport, accounting for first-principles electron-phonon scattering in a Lindbladian formalism. With increasing scattering strength, we identify three distinct regimes in the spin diffusion length: free induction decay, Dyakonov-Perel (DP) [12] and Elliott-Yafet (EY) [13, 14]. Most interestingly, the spin diffusion length is independent of scattering strength in the DP regime, with the overall dependence agreeing qualitatively, but not quantitatively, with the Einstein relation.

*Theory*—To incorporate spatial transport in real-time dynamics of the density matrix  $\rho$ , we use the Wigner function formalism to derive the spatial contribution to  $d\rho/dt$  in the local semi-classical limit as detailed in S.I. We combine the density-matrix quantum dynamics with spatial transport and explicitly account for electron-phonon scattering to obtain

$$\dot{\rho}_{n_1 n_2}^k(\mathbf{r}, t) = -\frac{\mathbf{v}_{kn_1} + \mathbf{v}_{kn_2}}{2} \cdot \nabla \rho_{n_1 n_2}^k(\mathbf{r}, t) \quad (1) \\ - \frac{i}{\hbar} [H', \rho]_{n_1 n_2}^k + L[\rho_{n_1 n_2}^k(\mathbf{r}, t)]$$

where  $\rho$  is the electronic density matrix in the interaction picture,  $\mathbf{v}_{kn}$  is the velocity of the state of wavevector  $k$  and band  $n$ . The first term is the spatial transport term and it implies that the off-diagonal matrix elements advect with the average velocity of the two states involved. The second term is the Liouville coherent evolution due to an additional perturbing Hamiltonian  $H'$ ,

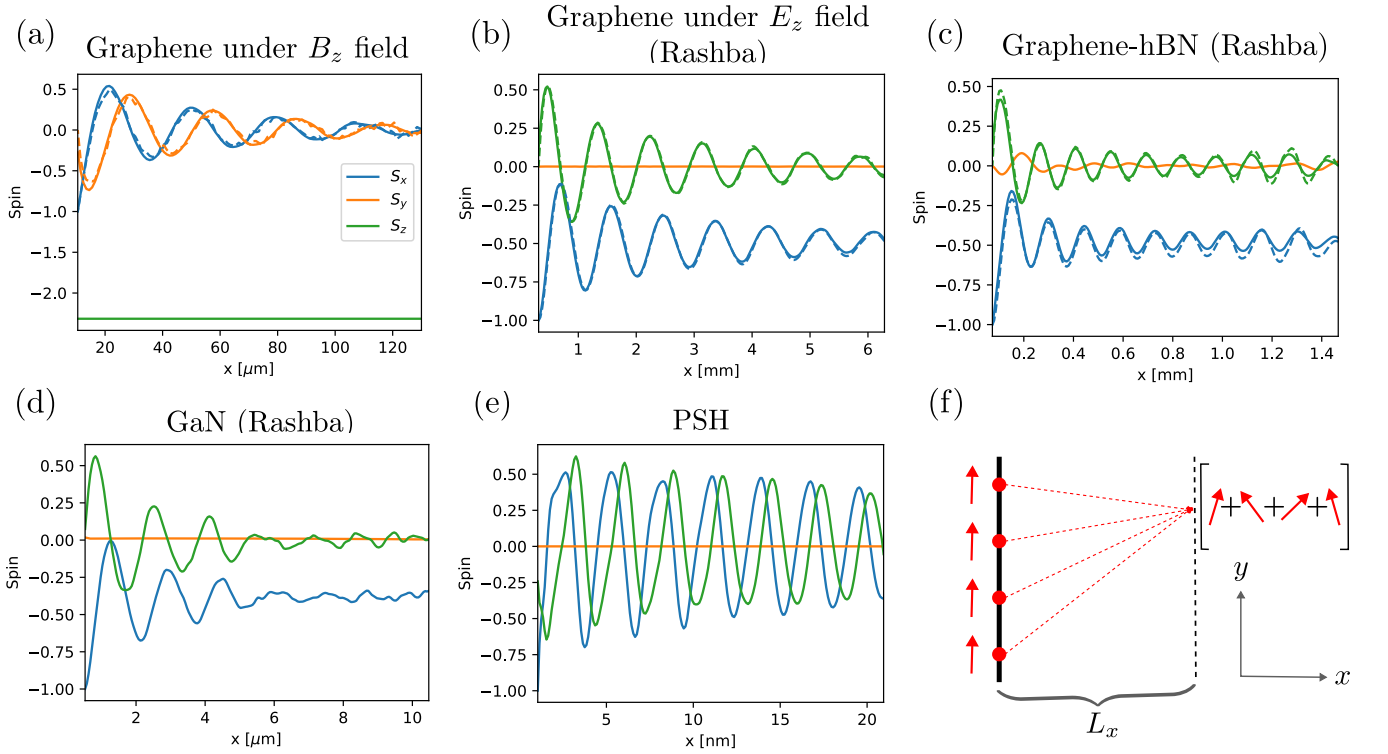


FIG. 1. The normalized average steady-state spin polarization in each direction as a function of the transport direction  $x$  for different materials, when  $x$ -spins are injected from the left contact. Spin dephasing due to spatial transport is observed in (a) graphene under an external magnetic field in the  $z$ -direction, (b) graphene under an external electric field in the  $z$ -direction (2D Rashba), (c) graphene-hBN (2D Rashba), (d) GaN (3D Rashba) and (e) hybrid perovskite (4,4-DFPD)2PbI4 with a persistent spin helix (PSH) spin texture. For (a), (b) and (c) the dotted lines compare corresponding analytical predictions. This transport dephasing is due to the different paths traveled by each electron illustrated in (f), where for transport along  $x$ -axis, as we initially have spins all in phase, after traveling a distance  $L_x$  while precessing, each spin has traveled a different path, and the spins are no longer in phase, leading to decrease in the average spin magnitude.

such as due to interactions with external fields. The third term is the Lindblad electron-phonon scattering given by

$$L[\rho_{n_1 n_2}^k(\mathbf{r}, t)] = \frac{2\pi}{\hbar N_q} \sum_{q\lambda \pm n'_1 n'_2 k'} n_{q\lambda}^{\pm} \times \text{Re} \left[ \begin{array}{c} (I - \rho^k)_{n_1 n'} A_{kn'; k' n'_1}^{q\lambda \pm} \rho_{n'_1 n'_2}^{k'} A_{k' n'_2; kn_2}^{q\lambda \mp} \\ -A_{kn_1; k' n'}^{q\lambda \mp} (I - \rho^{k'})_{n'_1 n'_1} A_{k' n'_1; kn'_2}^{q\lambda \pm} \rho_{n'_2 n_2}^k \end{array} \right] \quad (2)$$

where  $\pm$  indicates the absorption and emission of phonons with wave vector  $q = \mp(k - k')$  and mode index  $\lambda$ ,  $n_{q\lambda}^{\pm} \equiv n_{q\lambda} + \frac{1}{2} \pm \frac{1}{2}$ , and  $N_q = N_k$  is the total number of electron and phonon wave vectors sampled in the Brillouin zone.  $A_{kn'; k' n'_1}^{q\lambda \pm} = g_{kn'; k' n'_1}^{q\lambda \pm} \delta_G^{1/2}(\epsilon_{kn} - \epsilon_{k' n'} \pm \hbar\omega_{q\lambda}) \exp(i(\epsilon_{kn} - \epsilon_{k' n'})t)$ , where  $g_{kn'; k' n'_1}^{q\lambda \pm}$  is the electron-phonon matrix element, and the  $\delta_G$ -function is broadened to a Gaussian and applies energy conservation, where  $\epsilon_{kn}$  are the electron energies. The above has been obtained by tracing over the phonon degrees of freedom in the quantum Liouville equation and then applying the Born-Markov approximation in a form of Lindbladian dynamics for electronic system-phonon bath interactions[15].

*Coherent transport*—First, we start with ballistic transport in various materials with different spin textures, where we examine the spatial distribution of the average steady-state spin (Figure 1). The transport setup is 1D along the  $x$ -axis, where electron spins are polarized along the  $x$ -direction from the left contact by applying a magnetic field and leave the right contact. (See SI for details of the computational methods and simulation setup.)

We observe spin dephasing in the ballistic transport results without accounting for electron-phonon scattering yet, which is an effect of the spatial transport alone. This transport dephasing is due to the different path lengths traveled by each spin, as illustrated in Figure 1(f). For graphene under magnetic and electric fields and graphene-hBN, Figure 1(a), (b) and (c), the spin texture has a simple analytical form which leads to a corresponding analytical model for the transport that matches well with the numerical simulation results. To obtain the analytical solutions, we identify the directions of the external or internal magnetic field causing spin precession for electrons at each wavevector  $\vec{k}$  on the Fermi circle, compute the path length and net precession for that  $\vec{k}$ ,

and integrate over the Fermi circle (see SI.II for details). Figure 1(a) shows the transport in graphene, where there is a constant magnetic field on all spins. We also show how the transport profile changes for materials of various spin-orbit fields, where the internal effective magnetic field varies with electronic state. Graphene under an external electric field and graphene-hBN are examples of 2D Rashba, while GaN is a 3D Rashba material. Finally, (4,4-DFPD)2PbI4 in Figure 1(e) is an example of a persistent spin helix (PSH) material, where the dephasing is much weaker. In a perfect PSH material, the internal magnetic field is linearly dependent on only one direction in  $\mathbf{k}$  in such a way that the  $k$ -dependent precession frequency exactly compensates for the difference in path lengths. However, our first-principles simulations predict a weak transport dephasing in Figure 1(e) due to deviations of the internal magnetic field profile from the ideal PSH form.

For the results shown for the different graphene examples, we observe that as we look at the spin transport for longer length scales, a beat pattern is present. This is shown in Figure 2(a) for graphene under an external electric field, where the transport direction is along the  $x$  direction. However, this beat pattern is not present when the transport direction is along the  $y$  direction in Figure 2(b). This can be explained from Figure 2(c) which shows the velocity components  $v_x$  and  $v_y$  of the electrons at the Fermi circles  $K$  and  $K'$ . The two Fermi circles are not perfect circles, but distorted. This distortion causes the beat pattern because the electrons at  $K$  and  $K'$  are moving at noticeably different velocities. However, the beat pattern can be canceled for transport along certain directions. For the transport along  $y$ , the top half of the Fermi circle contributes to the transport. For the right side of the upper half, the electrons at  $K$  travel faster than those at  $K'$ , which causes a beat pattern. But it is canceled by an opposite beat pattern from the left side of the upper half. So there is no overall beat pattern in Figure 2(b) because there is no net bias between electrons at  $K$  vs  $K'$ . For the transport along  $x$ , the right half of the Fermi circle contributes to the transport, and it is divided into 3 regions, two of which cause beat patterns that cancel one another, while the central region has electrons at  $K'$  traveling faster than those at  $K$ . This leads to a net bias of  $K$  vs  $K'$  and a beat pattern as seen in Figure 2(a).

*Incoherent transport*—Now, we can add the Lindbladian scattering to the spin transport formalism to observe the effect of scattering to the spin transport profile. We will showcase this effect for graphene under an electric field. Before discussing the incoherent transport result with electron-phonon scattering, we first look at what happens to the spin life-time  $\tau_s$  as we change the scattering strength, controlled here by a scattering scale factor  $s$ . In Figure 3(a) we observe 3 different regimes of scattering, where the ballistic limit is at  $s \rightarrow 0$ . The free induction decay regime is where the scattering is very weak

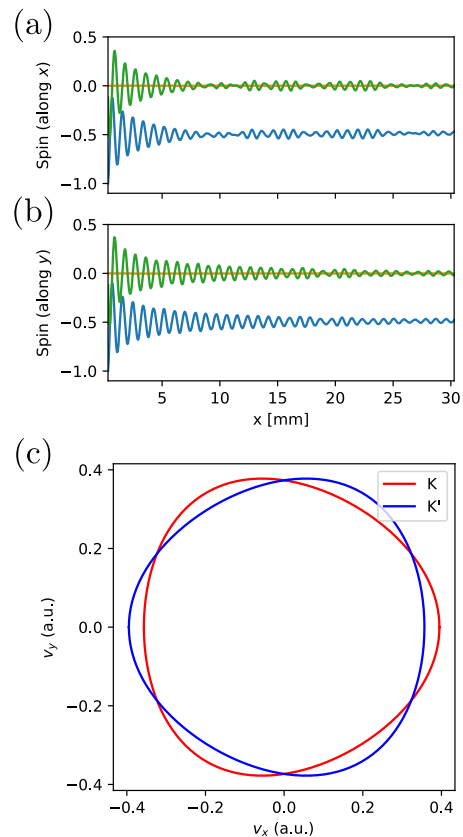


FIG. 2. (a,b) ballistic spin transport in graphene under an electric field in the  $z$  direction, where (a) shows a beat pattern for the transport along the  $x$  directions, while (b) shows transport along  $y$  direction without a beat pattern. (c) Velocity components  $v_x$  and  $v_y$  of the Fermi circles at  $K$  and  $K'$  are distorted from perfect circles due to deviation from the ideal Dirac cone shape at the chosen Fermi level  $\mu = 0.2$  eV away from the Dirac point. The electrons of  $K$  and  $K'$  with only  $x$  velocity components move at different velocities, leading to an interference in the spin precession profile and hence the beat pattern shown in (a). In contrast, electrons of  $K$  and  $K'$  with only  $y$  velocity components travel with the same velocity and show no beat pattern as seen in (b).

and  $\tau_s$  decreases as scattering increases. In this regime the spins precess many times before a scattering event happens. Once the scattering rate becomes comparable to and exceeds the precession rate, the Dyakonov-Perel (DP) regime begins, where  $\tau_s$  increases as the scattering increases. However, simultaneously, the spin flip rate due to spin mixing increases with increasing  $s$ , which eventually becomes the dominant mechanism at high  $s$ , leading to a switch to the Elliott-Yafet (EY) mechanism. In Figure 3(a), an analytical model (see SI) is plotted with the simulation result confirming the same behavior, where  $\Omega$  is the precession frequency and  $\tau_p$  is the momentum scattering lifetime. For large  $s$ , the first term goes as  $1/s$  and the second term goes as  $s$ , so the latter eventually takes over.

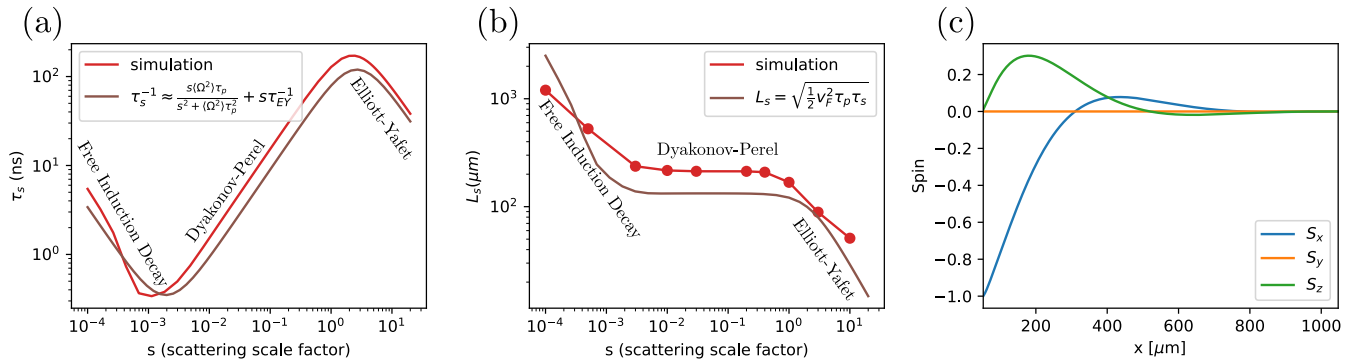


FIG. 3. (a) The spin lifetime  $\tau_s$  in graphene under an external electric field in the  $z$  direction, where it is calculated for varying scattering strengths controlled by scale factor  $s$ . Three different regimes are observed: free-induction decay, Dyakonov-Perel (DP) and Elliott-Yafet (EY). An analytical model is also plotted with simulation result to confirm the same behavior, where  $\Omega$  is the precession frequency and  $\tau_p$  is the momentum relaxation time. These three regimes are also observed in (b), where the spin diffusion length  $L_s$  from the spin transport simulations is plotted against the scattering strength. It is shown that in the DP region,  $L_s$  stays fixed as scattering strength changes. Using the relation  $L_s = \sqrt{D\tau_s}$ , where  $D$  is the diffusion coefficient given by the Einstein relation, shows the same behavior qualitatively, but we do not expect this relation to match quantitatively. (c) Incoherent spin transport including electron-phonon scattering, at scattering scale factor  $s = 1$ .  $x$ -spins are injected from the left contact, and a steady-state has been reached. The average spin magnitudes decay quickly compared with the ballistic case in Figure 1(b). The average spin magnitudes can be fitted to extract  $L_s$  at this specific  $s$ , which is repeated at different  $s$  to plot the simulation curve in (b).

The incoherent transport result with electron-phonon scattering is shown in Figure 3(c) for  $s = 1$ . Compared with the ballistic case in Figure 1(b), the scattering causes rapid decay in the average spin magnitudes. We can fit  $S_x$  and  $S_z$  to  $\cos(kx) \exp(-x/L_s)$  and  $\sin(kx) \exp(-x/L_s)$ , where  $k$  and  $L_s$  are the fitting parameters and  $L_s$  is the spin diffusion length. We repeat the incoherent transport simulation at various scattering scale factors, and fit each curve to obtain  $L_s$ . Figure 3(b) shows how  $L_s$  changes with scattering strength, where the free induction decay, DP and EY regimes are also observed. The analytical equation shown with the simulation result is the Einstein estimate and it is obtained by using the relation  $L_s = \sqrt{D\tau_s}$  [1], where  $D$  is the diffusion coefficient.  $D$  is given by the Einstein relation  $eD/\mu = mv^2/2$  where mobility  $\mu = e\tau_p/m$ . This estimate of  $L_s$  shows the same qualitative behavior as our simulation result, however we do not expect it to match quantitatively since there are quantitative differences in the first principles transport. A distinct feature in the DP region, is a constant  $L_s$  as the scattering strength changes. The Einstein estimate has the product  $\tau_p\tau_s$ , where  $\tau_s$  increases with scattering as seen in the DP region from Figure 3(a). Additionally, the momentum relaxation time  $\tau_p$  decreases with scattering, leading to the cancellation of both contributions leaving  $L_s$  constant. Results in Figure 3 are repeated for graphene-hBN (in SI), which shows constant  $L_s$  in the DP region as well. An incoherent transport simulation is done on silicon at  $s = 1$ , where  $L_s$  is found to be  $51.9\mu\text{m}$ . Using another form of the Einstein relation  $eD/\mu = k_B T$ , where  $k_B$  is the Boltzmann constant and  $T$  is the temperature,

$L_s$  now becomes  $L_s = \sqrt{\tau_s \mu k_B T / e}$ . At  $T = 100\text{K}$ ,  $L_s = 48.2\mu\text{m}$ . The spin transport curve showing the exponential decay can be found in SI.

*Conclusion*—To summarize, we have introduced a first principles density matrix technique with semi-classical spatial transport which simulates spatio-temporal spin dynamics and transport in realistic device geometries. This formalism also allows us to account for electron-phonon scattering from first principles at device length scales. We have shown coherent transport for different materials of different spin-orbit field profiles, where dephasing is observed as an effect of spatial transport alone. Additionally, we have shown incoherent transport in graphene under an electric field as an example of spatial transport with a nearly ideal Rashba spin texture. We have shown that the variation of spin diffusion length with scattering strength exhibits three distinct regimes: free induction decay, DP and EY, with a notable scattering-strength-independent spin diffusion length in the DP regime, in qualitative agreement with the Einstein relation. We have demonstrated that our *ab initio* technique is general and not constrained to specific parameterizations of electronic Hamiltonians or phonon models, allowing us to study spin dynamics and transport with first-principles electron-phonon scattering for a wide range of materials.

*Acknowledgments*—This work is supported by the Computational Chemical Sciences program within the Office of Science at DOE under Grant No. DE-SC0023301. Calculations were carried out at the National Energy Research Scientific Computing Center (NERSC), a U.S. Department of Energy Office of Science User Facility op-

erated under Contract No. DEAC02-05CH11231, as well as at the Center for Computational Innovations (CCI) at Rensselaer Polytechnic Institute.

---

\* yping3@wisc.edu

† sundar@rpi.edu

- [1] J. Fabian, A. Matos-Abiague, C. Ertler, P. Stano, and I. Žutić, Semiconductor spintronics, *Acta Physica Slovaca. Reviews and Tutorials* **57**, 10.2478/v10155-010-0086-8 (2007).
- [2] J. H. Garcia, M. Vila, A. W. Cummings, and S. Roche, Spin transport in graphene/transition metal dichalcogenide heterostructures, *Chem. Soc. Rev.* **47**, 3359 (2018).
- [3] Y. Xue, S. Datta, and M. A. Ratner, First-principles based matrix green's function approach to molecular electronic devices: general formalism, *Chemical Physics* **281**, 151 (2002).
- [4] S. Y. Quek and K. H. Khoo, Predictive dft-based approaches to charge and spin transport in single-molecule junctions and two-dimensional materials: Successes and challenges, *Accounts of Chemical Research* **47**, 3250 (2014), doi: 10.1021/ar4002526.
- [5] H. Sadeghi, Theory of electron, phonon and spin transport in nanoscale quantum devices, *Nanotechnology* **29**, 373001 (2018).
- [6] R. J. H. Wesselink, K. Gupta, Z. Yuan, and P. J. Kelly, Calculating spin transport properties from first principles: Spin currents, *Physical Review B* **99**, 144409 (2019).
- [7] A. W. Cummings, S. M.-M. Dubois, J.-C. Charlier, and S. Roche, Universal spin diffusion length in polycrystalline graphene, *Nano Letters* **19**, 7418 (2019), doi: 10.1021/acs.nanolett.9b03112.
- [8] J. Xu, A. Habib, S. Kumar, F. Wu, R. Sundararaman, and Y. Ping, Spin-phonon relaxation from a universal ab initio density-matrix approach, *Nature Communications* **11**, 2780 (2020).
- [9] J. Xu, A. Habib, R. Sundararaman, and Y. Ping, *Ab initio* ultrafast spin dynamics in solids, *Physical Review B* **104**, 184418 (2021).
- [10] A. Habib, J. Xu, Y. Ping, and R. Sundararaman, Electric fields and substrates dramatically accelerate spin relaxation in graphene, *Phys. Rev. B* **105**, 115122 (2022).
- [11] J. Quinton, M. Fadel, J. Xu, A. Habib, M. Chandra, Y. Ping, and R. Sundararaman, Magnetic-field dependence of spin-phonon relaxation and dephasing due to  $g$ -factor fluctuations from first principles, *Physical Review B* **111**, 115113 (2025).
- [12] M. Dyakonov and V. Perel, Spin relaxation of conduction electrons in noncentrosymmetric semiconductors, *Sov. Phys. Solid State* **13**, 3023 (1972).
- [13] R. J. Elliott, Theory of the effect of spin-orbit coupling on magnetic resonance in some semiconductors, *Physical Review* **96**, 266 (1954).
- [14] Y. Yafet,  $g$  factors and spin-lattice relaxation of conduction electrons, in *Solid state physics*, Vol. 14 (Elsevier, 1963) pp. 1–98.
- [15] D. Taj, R. C. Iotti, and F. Rossi, Microscopic modeling of energy relaxation and decoherence in quantum optoelectronic devices at the nanoscale, *The European Physical Journal B* **72**, 305 (2009).